Tin Dioxide-Based Photoanodes Integrated Into the Dye Sensitized Solar Cells Structure

Francisco Marcone Lima[a,b] ⓘ, *Juliana Sales O. Leitão[a,c]* ⓘ, *Vanja Fontenele Nunes[b]* ⓘ,

Michel Rodrigues Andrade[d], João Pedro Santana Mota[b], Thiago Alves de Moura[e],

Ana Fabíola Leite Almeida[b] ⓘ, *A. F. Valentim de Amorim[a], Daniel de C. Girão[a,f]* ⓘ,

Francisco Nivaldo Aguiar Freire[b], Janaína Sobreira Rocha[a,c]* ⓘ

[a]*Núcleo de Tecnologia e Qualidade Industrial do Ceará, Grupo de Nanotecnologia e Materiais Avançados, Fortaleza, CE, Brasil.*
[b]*Universidade Federal do Ceará, Laboratório de Filmes Finos e Energias Renováveis, Fortaleza, CE, Brasil.*
[c]*Universidade Federal do Ceará, Grupo de Química de Materiais Avançados, Fortaleza, CE, Brasil.*
[d]*Universidade Federal do Ceará, Fortaleza, Grupo de Teoria da Matéria Condensada, Fortaleza, CE, Brasil.*
[e]*Instituto Federal de Educação, Ciência e Tecnologia do Ceará, Acaraú, CE, Brasil.*
[f]*Universidade Federal do Ceará, Laboratório de Pesquisa em Corrosão, Fortaleza, CE, Brasil.*

This academic article investigates the performance of dye-sensitized solar cells (DSSCs), which are affected by various defects like charge recombination, high impedance, and low power conversion efficiency due to complex physicochemical phenomena. The study explores different materials and processes to enhance DSSC performance, with a focus on photoanode development. Tin dioxide, tin chloride II dihydrate, copper oxide, boric acid, and sodium phosphate are utilized to fabricate the photoanodes. A thermal treatment at 450°C for 30 minutes precedes dye assembly on the photoanode surface. Results show that the tin chloride II dihydrate-modified photoanode outperforms others, achieving higher open-circuit voltage (0.50V), current density (9.58 mAcm^{-2}), fill factor (0.37), and power conversion efficiency (1.77%). The study suggests that tin salt particles positively impact voltage, current, electron transport, and charge separation, enhancing overall cell performance. Charge recombination significantly affects power conversion efficiency and impedance, but accurately quantifying it remains challenging. Lower recombination levels favor efficiency, while higher levels reduce it.

Keywords: *Photoanodes, solar cells, tin dioxide.*

1. Introduction

Dye-sensitized solar cells (DSSCs) feature a sandwich-type architecture comprising a dye-sensitized photoanode, an electrolyte, and a counter electrode structure[1-38]. Within DSSCs, the photoanode governs photocurrent via the quantity of immobilized dye and voltage through the potential gradient between the Fermi level at the interface between the photoanode and the electrolyte[14]. The observed low voltage and electrical current in DSSCs are attributed to charge recombination occurring within the cell, influenced by the layers in the sandwich-type architecture. The values for charge recombination vary across the layers during the photovoltaic process in DSSCs, making their calculation difficult. However, the effect of this variation can be analyzed through the electrical parameters of current, voltage, fill factor, and efficiency. Generally, lower levels of charge recombination enhance these electrical parameters, while higher levels reduce them. Additionally, some authors represent solar cell power generation using a coordinate system where current density and/or voltage values are negative, while others use positive values. However, the study of coordinate systems

for representing solar cell power generation is beyond the scope of this work.

Among the different components and processes in DSSCs, the selection of the photoanode type is crucial due to its significant impact on the resulting performance. Various materials have been considered for the development of photoanodes, including TiO2/GO/Ag nanofibers[28], TiO2/MnO$_2$ bilayer-assembled photoanode[30], spinel oxide-incorporated photoanode[31], ruthenium-based double dyes incorporated photoanode[32], reduced graphene oxide and carbon nanotubes in ZnO nanostructures[33], lithium incorporation into TiO$_2$ photoanode[34], rGO-incorporated TiO$_2$ photoanode[35], and CuO:TiO$_2$ nanocomposites photoanode[36]. These endeavors have significantly contributed to the advancement of photoanode research for DSSCs, providing valuable insights for future investigations. However, the challenge of producing photoanodes capable of minimizing charge recombination remains a hurdle to be addressed.

Titanium dioxide (TiO$_2$), a semiconductor with a large bandgap, has long served as the traditional photoanode material for DSSCs. In a pioneering study, O'Regan and Grätzel utilized TiO$_2$ nanoparticles modified by titanium

*e-mail: janaina.sobreira@nutec.ce.gov.br

trichloride, followed by thermal treatment at 450°C for 30 minutes, achieving a remarkable 7.9% power conversion efficiency (PCE)[1]. This marked a significant milestone as, up until that point, it represented the highest reported efficiency for DSSCs, igniting widespread interest and research contributions from scientists worldwide.

As of the time of writing, the highest reported PCE for DSSCs stands at 15.2%[37], marking a substantial improvement. According to the authors, this enhanced performance is attributed to the precise control of dye molecule packing facilitated by a monolayer of a hydroxamic acid derivative pre-adsorbed onto the surface of nanocrystalline mesoporous TiO_2, which promotes efficient charge generation.

As charge recombination within the photoanode significantly impacts the voltage and electrical photocurrent, leading to decreased DSSC efficiency, considerable efforts are being made to find efficient photoanodes. Various photoanode architectures have been explored to enhance electron transfer, light conversion, and ion diffusion at the semiconductor-electrolyte interface within DSSCs. Among these architectures, the use of dye-sensitized tin dioxide (SnO_2) semiconductor as a photoanode has been reported in the literature as an alternative material to titanium dioxide TiO_2[14]. SnO_2 photoanodes have the potential to enhance DSSCs due to their larger band gap of 3.8 eV compared to 3.2 eV for TiO_2. This difference can result in the generation of fewer oxidative holes in the valence band under ultraviolet radiation, thereby reducing the rate of dye degradation in DSSCs[6]. In studies of electronic structure, the Kubelka-Munk method has been reported as a useful tool for determining the SnO_2 band gap from optical reflectance[38], while Raman spectroscopy has been utilized to investigate the crystal structure[39,40].

The high recombination of charges in SnO_2-based photoanodes poses a challenge for their development and application in DSSCs. To address this issue, various parameters have been adjusted in the development of SnO_2-based photoanodes. SnO_2 powder was synthesized from tin chloride through sintering at 500°C. Subsequently, the SnO2 layer was treated at 450°C for 30 minutes to serve as a photoanode, resulting in DSSCs with a current density (J_{sc}) of 3.975 mAcm^{-2}, an open-circuit voltage (V_{oc}) of 0.32 V, a fill factor (FF) of 0.3559, and a power conversion efficiency (PCE) of 0.3592%[11]. The authors did not report the type of dye used; instead, their focus was on the preparation method of SnO_2 nanoparticles using a tin Schiff base complex.

Various structures of SnO_2 photoanodes have been incorporated into DSSC structures using commercially available ruthenium-based dyes to enhance photogenerated current density and cell voltage. The performance of N3-dye sensitized solar cells (N3-DSSC) varied depending on the photoanode structure: SnO_2 (J_{sc} = -8.0 mAcm^{-2}, V_{oc} =0.36 V, FF =48%), SnO_2:ZnO(J_{sc} = - 9.2 mAcm^{-2}, V_{oc} = 0.58 V, FF =67%) and SnO_2:ZnO:Nb_2O_5 (J_{sc} =-7.1 mAcm^{-2}, V_{oc} =0.58 V, FF =69%)[8]. The authors observed that the amount of SnO_2, ZnO, and Nb_2O_5 in photoanode affects the solar cell performance. Similar behavior was observed in N719-DSSC with photoanodes of SnO_2 (J_{sc} = 2.21 mAcm^{-2}, V_{oc} =0.54993 V, FF = 57.38%), SnO_2: (1wt%)Li-ZnO (J_{sc} = 4,73mAcm^{-2}, V_{oc} =0.63015 V, FF = 69.33%) and SnO_2: (0.5t%)Li-ZnO (J_{sc} = 4,73mAcm^{-2}, V_{oc} =0.63015 V, FF = 69.33%)[16]. Also, in N719-DSSC with photoanodes of SnO_2:TiO_2 (J_{sc} = 5.735 mAcm^{-2}, V_{oc} =0.64 V, FF =45%) SnO_2:TiO_2:(0.45wt%)grapheme oxide(J_{sc} = 10.185 mAcm^{-2}, V_{oc} =0.67 V, FF =46%) and SnO_2:TiO_2:(4.75wt%)grapheme oxide(J_{sc} = 10.185 mAcm^{-2}, V_{oc} =0.67 V, FF =46%)[18].

Combinations of SnO_2 with chemical elements have been utilized to enhance the electrical potential gradient between modified SnO2 and the electrolyte[14]. When SnO2 was paired with nickel oxide (NiO) as a photoanode and [N-bis(2-20-bipyridyl-4,40-dicarboxylic acid)] Ru(II) dye, the resulting DSSC generated Jsc = 8.6 mAcm^{-2}, Voc = 0.51 V, and PCE = 2.7%. In contrast, DSSCs without the modified photoanode exhibited Jsc = 2.8 mAcm^{-2}, Voc = 0.33 V, and PCE = 0.5%[2]. The superior performance was attributed to the semiconductor nature of NiO, which is of p-type, thereby facilitating the creation of a local p-n junction. This enhancement resulted in an over five-fold increase in cell conversion efficiency.

Dye-sensitized solar cells (DSSCs) employing SnO_2 nanosheets and zinc oxide (ZnO) as the photoanode, treated at 400°C, exhibited a photocurrent density (Jsc) of 2.65 mAcm^{-2}, an open-circuit voltage (Voc) of 0.62 V, and a power conversion efficiency (PCE) of 0.54%. The elevated voltage is attributed to the presence of ZnO. DSSCs employing SnO_2 and calcium carbonate ($CaCO_3$) as the photoanode, along with N719 dye, demonstrated efficiencies ranging from 2.3% to 5.4%. The impact of varying efficiency was elucidated as a function of the amount of $CaCO_3$, while a PCE of 1.7% was achieved for the DSSC utilizing unmodified SnO_2[3]. Additionally, the influence of the dye on DSSCs employing the SnO_2 photoanode was investigated. In the last two works, the authors adopted a coordinate system in which current is negative, with more negative values associated with greater charge generation.

Despite substantial work by the community to advance DSSCs, there is currently no published data, to the author's knowledge, on SnO_2-based photoanode arrays modified with tin chloride II dehydrate ($SnCl_2.2H_2O$) obtained from natural sedimentation and subsequent thermal treatment, and with the addition of copper oxide (CuO), boric acid (HBO_3), and sodium phosphate (Na_2HPO_4) powder layers before sealing the DSSCs. The photovoltaic characteristics of DSSCs with modified SnO_2 photoanodes were investigated using current-voltage density (J-V) and photoelectrochemical impedance spectroscopy. In this work, the authors utilized SnO_2-based photoanodes as a starting point to examine the compatibility of electrical parameters as a tool for the indirect analysis of charge recombination throughout the layers during the photovoltaic process in DSSCs.

2. Experimental

2.1. Preparation of the photoanode

The fabrication process for the photoanodes began with the cleaning of transparent conductive oxides (TCOs) containing fluorine-doped tin oxide coating, with a sheet electrical resistance of 17.60 ohm/sq. The cleaning procedure involved subjecting the TCOs to an ultrasound bath for 10 minutes, using a mixture of water and ethyl alcohol in

equal volumes. Two different processes were employed for the assembly of SnO_2-based photoanodes.

In the first process, 0.084g of SnO_2 and an amount of tin salt equivalent to 16 percent of the SnO_2 mass were added to approximately 10 mL of distilled water. The mixture underwent ultrasonic treatment for 30 minutes with stirring. The resulting suspension was then added to a reactor containing a transparent conductive oxide (TCO) substrate measuring 1.00 cm x 2.5 cm. The setup was left for evaporation by natural convection for 7 days, after which the photoanodes were thermally treated at 450°C for 30 minutes. Following thermal treatment, the photoanodes were coated with N719 dye, completing the assembly process. This assembly is referred to as S:S. In the absence of tin salt, a similar procedure was followed, and the resulting photoanode is referred to as S.

In the second process, a powder layer of CuO (S:C), HBO_3 (S:B), and Na_2HPO_4 (S:NP) was deposited on top of each SnO_2 photoanode (S). The amount of these materials was equivalent to 16 percent of the mass of SnO_2. The deposition onto S was performed using a 72 micrometer hole sieve, without subsequent thermal treatment.

2.2. DSSCs assembly

The open cell sandwich structure (photoanode/dye/ electrolyte/counter electrode) with an active area of 0.50 cm^2 was adopted. For dye immobilization onto the photoanodes to obtain the S and S:S photoanodes, they were immersed in equal volumes of an ethyl alcohol solution containing 3.0×10^{-4} M of Ruthenizer 535-bisTBA (N719) dye and 0.3×10^{-4} M of chenodeoxycholic acid additive. Commercial counter electrodes containing fluorine-doped tin oxide (FTO) with platinum coating were used. The FTO type TCO, counter electrodes, and Iodolyte AN-50 electrolyte were purchased from Solaronix (Switzerland).

2.3. Characterizations

The diffuse reflectance spectra of the photoanodes were measured using a UV-2600 Shimadzu spectrophotometer equipped with an integrating sphere ISR-2600Plus. The band gap of the photoanodes was determined using the Kubelka-Munk method with diffuse reflectance data[38].

For X-ray diffraction measurements, the Panalytical X'Pert PRO diffractometer - model MPD - was used, using cobalt radiation (λ = 1.78896Å) and operating at 40 kV and 40 mA. The geometry used was parallel beam using a monochromator and a 1/4° slit. The sample holder was mounted on a spinner and the geometry of the diffracted beam consisted of a 0.02° soller slit. The range was from 6° to 100° with a step of 0.013°.

The Raman Raman Spectroscopy analyses were performed using an Alpha 300 system from Witec (Ulm, Germany) working with a 20x Nikon objective, and with Nd:YAG (532 nm) laser excitation. The Raman signal analysed throught a high-sensitivity, back illuminated CCD located behind a 600 l/mm grating. For each sample, the Raman spectrum was accquired throught 3 accumulations of 10 seconds each with a laser intensity of 5 mW.

The AFM analyses were performed using a Asylum MFP 3D (Oxford instruments) working in non-contact (tapping) mode with a silicon tip (NCHR-W, Nano World) mounted in

a cantilever of 4 µm thicknes, 125 µm lenght, 30 µm width, 320 kHz resonance frequency and 42 N/m force constant. For each sample, it was sccaned a 30 µm x 30 µm area.

The cells were characterized using a potentiostat/galvanostat PGSTAT302N (Metrohm, Switzerland) to obtain current density (J) versus voltage (V) curves and electrochemical impedance spectroscopy (EIS) characteristics. Both J-V and EIS measurements were conducted under simulated solar illumination using white LED light sources with an intensity pattern of 100 mW/cm². For impedance measurements, the conditions included a frequency interval from 100 kHz to 1 Hz, a signal amplitude of 10 mV, and the open-circuit voltage (V_{oc}).

3. Results and Discussion

3.1. Structural characterization of prepared materials

Figure 1 and Figure 2 depict X-ray diffraction (XRD) patterns of the S and S:S photoanodes, respectively, after calcination for 30 minutes at 450°C, with diffraction patterns indexed to Sn-based clusters.

Taking Figure 1, the XRD patterns[41-45] match well with the superlattice $(SnO_2)_1(SnO_2)_1$ (COD 1000062), which is the dominant phase identified in the SnO_2-based photoanodes. However, the identification of a secondary phase represented by $(SnO_2)_1(SnO.12O_2)_1$ (COD 1533658) is observed as a byproduct of the material's calcination.

On the other hand, in Figure 2, all diffraction peaks were perfectly indexed to the superlattice $(SnO_2)1(SnO_2)1$ (COD
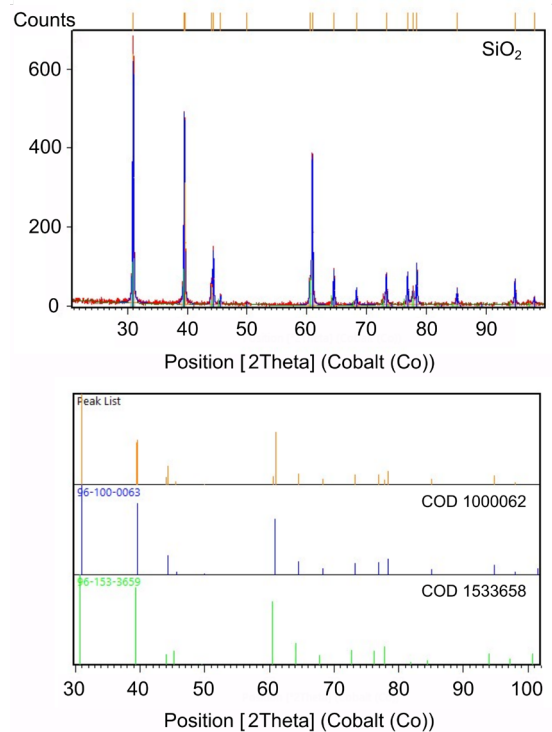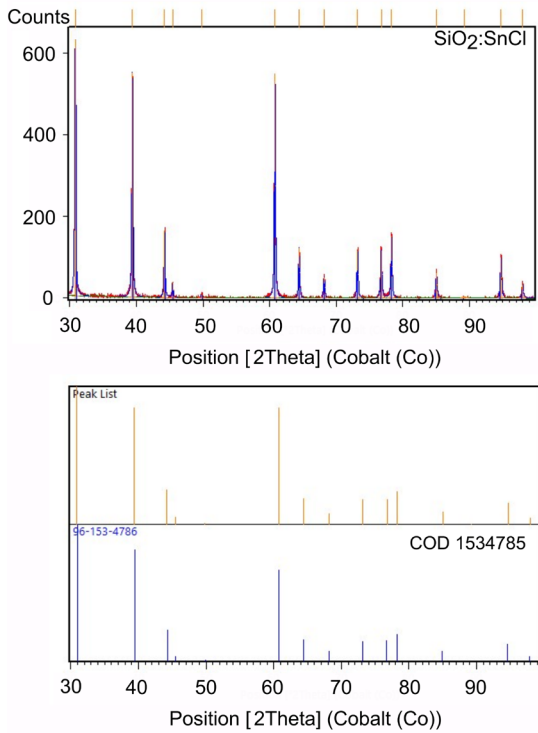

**Figure 1.** X-ray diffraction (XRD) patterns of S photoanodes.

1534785) without the presence of other phases. Possibly, the addition of tin salt contributes to the absence of a secondary phase in the S:S photoanode

Raman spectroscopy measurements were performed for all prepared samples (Figure 3).

In the SnO_2 sample, the typical spectrum of this material is observable[46-49], with the presence of bands at 476 cm^{-1} (Eg), 635 cm^{-1} (A_{1g}), and 775 cm^{-1} (B_{2g}). These bands correspond to the fundamental phonon modes Eg, A_{1g}, and B_{2g}, respectively,

Figure 2. X-ray diffraction (XRD) patterns of S:S photoanodes.
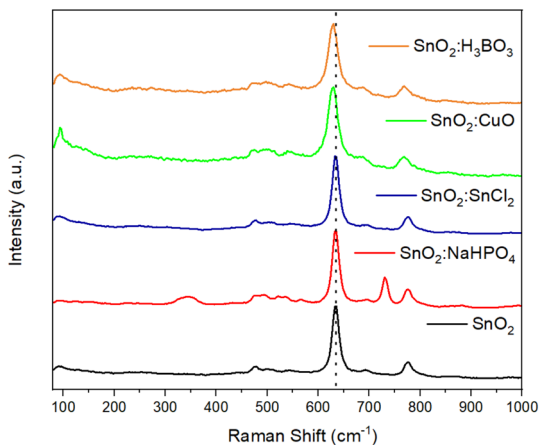
Figure 3. Raman spectra of the SnO2, SnO2:NaHPO4, SnO2:SnCl2, SnO2:CuO, and SnO2:H3BO3 samples.

in good agreement with those observed in pure SnO_2. These active modes are in good agreement with the standard rutile tetragonal SnO_2 structure as reported in earlier literature, where the non-degenerate Raman modes A_{1g} and B_{2g} denote the contraction and expansion of the vibrational mode of Sn – O bonds, while the doubly degenerate Eg mode is related to the vibration of oxygen in the oxygen plane.

In the SnO_2:$NaHPO_4$ sample, the formation of bands at 345 and 731 cm^{-1} is observable, while in the SnO_2:$SnCl_2$, SnO_2:CuO, and SnO_2:H_3BO_3 samples, a shift of the 627 cm^{-1} band present in the pure SnO_2 sample is observed, indicating that in all synthesized samples, an interaction of the SnO_2 compound with the present salts was observed.

It is important to emphasize that the incorporation of these salts in powder form and their distinct granulometries can alter the behavior of the formed cells. High porosity may lead to the infiltration of a high concentration of dye into the inner layer, promoting electrical resistance, while low porosity may result in dye accumulation in superficial regions of the cell, also acting as regions of electrical resistance.

However, the images obtained by Atomic Force Microscopy (AFM) (Figure 4) of the analyzed samples[47,50] reveal the formation of a porous final material with minimal differences in porosity among them, indicating that the insertion of salts did not cause significant changes in their surface porosities.

3.2. Photovoltaic performance by J-V

Figure 5 depicts the current density-voltage values for DSSCs with various compositions of SnO_2-based photoanodes under an illumination intensity of 100 mW/cm^2. Notably, among the cells, only DSSC S:S (as listed in Table 1) exhibits both high V_{oc} and J_{sc}, attributed to enhanced charge separation facilitated by particles generated from $SnCl_2$.$2H_2O$.

Table 1 lists the main parameters (J_{sc}, V_{oc}, FF, PCE, parallel (R_{shunt}), and series ($_{series}$) resistances) studied in the literature as tools to investigate the photovoltaic performance of solar cells.

R_{series} represents all the ohmic resistances contributing to energy loss in the cell as heat, while R_{shunt} represents potential charge recombinations within the cell. When comparing the R_{series} and R_{shunt} values listed in Table 1, it becomes evident that cells with higher R_{series} values tend to exhibit lower efficiency due to increased energy loss. Additionally, the comparison between R_{shunt} and Rseries values for the S:S cell and other cells highlights a direct relationship between R_{series} loss and R_{shunt} gain, indicating a dependency on the materials present in the photoanode.

The photovoltaic parameters (V_{oc}, J_{sc}, and fill factor) of the S, S:S, and S:C cells exhibit similarities with parameters reported in the literature for DSSCs incorporating tin dioxide-based photoanodes through various strategies. For instance, DSSCs with SnO_2 and N719 dye as the photoanode have been reported to exhibit R_{series} = 19 Ω.cm[2] and Rshunt = 114 Ω.cm[2], with Jsc = 4.74 mA cm^{-2}, Voc = 0.36 V, FF = 0.3140, and PCE = 0.53%[24]. Similarly, for DSSCs with SnO_2-ZnO-Nb_2O_5 and N719 dye as the photoanode and iodide/triiodide electrolyte, higher values were reported, with Jsc = -8.1 mA cm^{-2}, Voc = 0.54 V, and FF = 0.65[8]. The enhanced V_{oc} and FF in the latter case were attributed to the inclusion of ZnO and Nb_2O_5.

**Table 1.** Photovoltaic characteristics for the SnO_2-based Photoanodes DSSCs.

Photoanodes	DSSC	V_{oc}(V)	J_{sc}(mA/cm^2)	FF	PCE (%)	R_{series} ($\Omega.cm^2$)	R_{shunt} ($\Omega.cm^2$)
SnO_2	**S**	0.26	3.71	0.31	0.30000	1248.80	990.60
SnO_2:$SnCl_2$	**S:S**	0.50	9.58	0.37	1.77000	1226.00	998.20
SnO_2 :CuO	**S:C**	0.67	2.93	0.40	0.79000	1053.60	998.10
SnO_2:H_3BO_3	**S:B**	0.09	2.27	0.27	0.05600	2166.70	974.00
SnO_2:Na_2HPO_4	**S:NP**	0.03	0.12	0.29	0.00087	3146.80	878.70
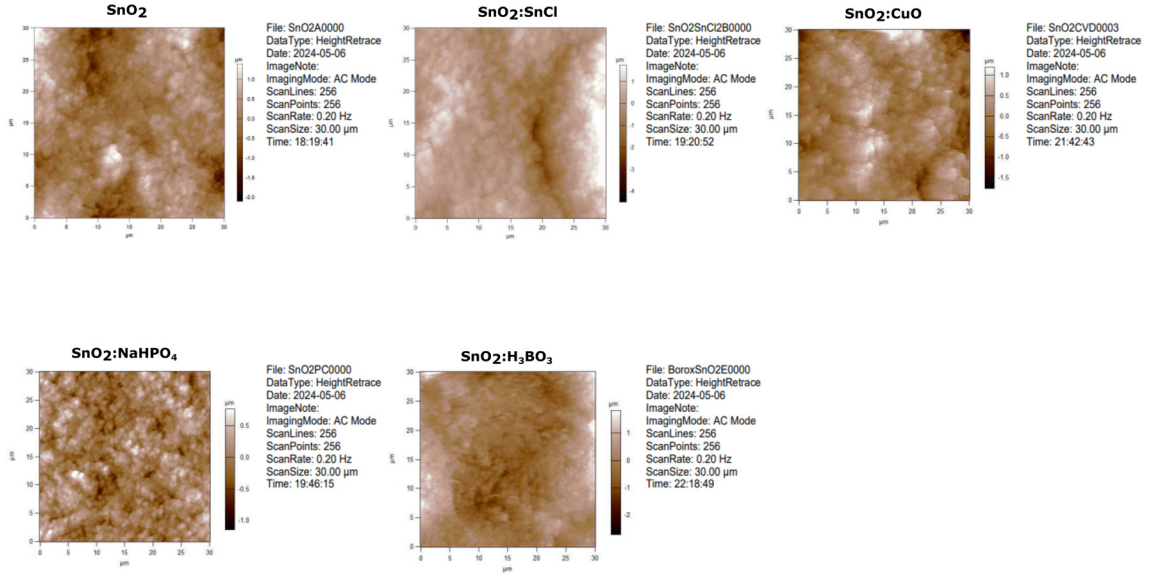
Figure 4. Atomic Force Microscopy (AFM) images for all prepared materials.

Replacing the N719 dye with the SnO_2-ZnO-Nb_2O_5 and N3 ruthenium-based dye as the photoanode resulted in changes in the photovoltaic parameters of the DSSCs. Specifically, the values became Jsc = -5.2 mA cm^{-2}, Voc = 0.53 V, and FF = 0.54[8]. Similarly, Chen and collaborators produced DSSCs based on SnO2 and cis-bis(thiocyanato)-N,N-bis(2,2-bipyridyl-4,4-dicarboxylate) ruthenium (II) or N3 dye as photoanodes, with an electrolyte iodide/triiodide couple, resulting in J_{sc} = 2.96 mA cm^{-2}, V_{oc} = 0.299 V, FF = 0.32, and PCE = 0.28%. Moreover, DSSCs with the SnO_2 photoanode and ruthenium-based dye were reported with photovoltaic parameters of V_{oc} = 0.32 V, J_{sc} = 3.795 mA cm^{-2}, FF = 0.32, and PCE = 0.3952%[11]. These findings highlight the influence of all layers in the sandwich structure on the performance of the DSSC.

The use of $SnCl_2.2H_2O$ as an additive for modifying SnO_2-based photoanodes has notably improved the photovoltaic performance of the cell, as evident in Table 1 and Figure 5. This improvement can be attributed to the effective complementarity between the reduction in charge recombination, as indicated by the increase in Rshunt, and the decrease in ohmic resistance induced by the additive on the SnO_2-based photoanode, particularly in the S:S cell. This relationship significantly influences all current and voltage data, resulting in the observed plots in Figure 5.
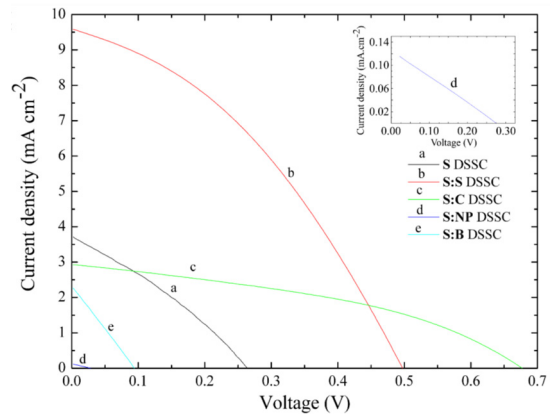
Figure 5. J-V characteristics for the DSSCs with SnO2-based photoanodes.

Due to the lower Fermi level of SnO_2 compared to TiO_2 semiconductor, DSSCs based on pure SnO_2 photoanodes activated with iodide/triiodide redox electrolyte typically exhibit V_{oc} values below 0.5 V[2-4,8,11,14], whereas TiO_2 photoanodes yield Voc around 0.7 V[14]. Consequently, extensive research has

been conducted to enhance the Voc of SnO_2-based photoanode DSSCs. Methods explored include the addition of organic and inorganic additives, alterations in dye composition, and modifications to the electrolyte. In this study, high voltage was achieved through the incorporation of $SnCl_2$ and CuO as inorganic additives, while N719 acted as the organic additive to enhance photocurrent gain.

Initially, under luminous energy, solar cells generate electrons, and as these electrons migrate (photocurrent) within the cell, a layer begins to form and captures the free electrons. This leads to the formation of a junction with layers of opposite charges, which is responsible for generating the cell voltage. In DSSCs, recombination occurs at the interface of the photoanode with the immobilized dye and the electrolyte. To achieve higher values of luminous energy to photovoltaic electricity conversion, the increase in voltage must be balanced by the generation of free electrons with high energy. The behavior observed, particularly in the S:S cell (Table 1), suggests appropriate generation of high potential at the interface of the modified SnO_2 and the electrolyte, albeit with a high concentration of electrons.

In the S:C DSSC, the high V_{oc} value of 0.67 V and the low J_{sc} value of 2.93 mA cm^{-2} indicate an incompatibility between voltage increase and the generation of free electrons with high energy. While the presence of copper atoms (Cu) contributes to the increase in cell voltage, the high capture of free electrons leads to a decrease in J_{sc}. Conversely, for the S:NP and S:B cells, modification of the SnO^2 photoanodes results in a decrease in cell voltage and high capture of free electrons. However, the opposite effect is observed for the S:S cell, leading to higher efficiency. This suggests that the modification in the S:S configuration yields a balance between voltage increase and generation of free electrons, resulting in improved cell performance.

The fill factor (FF) serves as an indicator of the stability of solar cells in generating electrical energy under illumination. It represents the cell's resistance to energy loss when subjected to an electric field induced by the accumulation of charge in the presence of luminous energy. This stability can be illustrated through a simple experiment: when a photovoltaic cell is connected to a data collector focused on luminous energy, the product of each current density (J) and its associated voltage (V) is calculated (Figure 5). Among these values, one stands out as the maximum energetic product, representing the peak energy produced by the cell. However, beyond a certain voltage threshold, the energy product (J x V) sharply decreases from the maximum energy product (J x V)$_{max}$ (Figure 5).

Beyond a specific voltage threshold, less stable cells exhibit electrons with lower energy than the electric field produced by the accumulation of charge (EAC). Consequently, these electrons are captured from the EAC rather than being accelerated. The fill factor (FF) is determined by the ratio of the maximum energy product (J x V)$_{max}$ to the ideal energetic product (J_{sc} x V_{oc}). A FF closer to unity indicates higher cell stability in the presence of luminous energy. The lower FF values presented in Table 1 indicate a high concentration of electrons with energy below that of the electric fields induced in SnO_2-based photoanode cells, both modified and unmodified. However, these FF values are consistent

with those reported in the literature for SnO_2 photoanodes, whether modified or unmodified.

The superior photovoltaic performance of the S:S DSSC, characterized by a PCE of 1.77% and J_{sc} of 9.58 mA.cm^{-2}, suggests an optimal concentration of tin (Sn) on the modified SnO_2 photoanode. Notably, the Jsc value of 9.58 mA.cm^{-2} surpasses that of other DSSCs, while the Voc value of 0.50 V is second only to that associated with the S:C DSSC. These results can be attributed to the effective capture of excess electrons in the conduction range of SnO_2. As these electrons accumulate, there is an upward and forward shift in the conduction band fringe at the SnO_2-SnO_2 modified grain boundary. This shift generates a high potential at the interface of the modified SnO_2 and the electrolyte, facilitating the injection of electrons from the energy level of the dye to the energy level of the SnO_2 modified with tin atoms, thereby promoting charge separation. The observed differences in open circuit voltage among the experimental samples were further investigated using spectroscopy of electrochemical impedance (EIS) applied to DSSCs under illumination.

3.3. Electrons transport characteristics in the DSSC estimated by EIS

In studying the behavior of photoelectron injection and charge recombination in DSSCs, electrochemical impedance spectroscopy (EIS) is a valuable tool applied to solar cells[9,10,12,13,16,17,23,27]. This analysis focuses on the impedance of the cell, which comprises several components. Specifically, the total impedance (Z) encompasses the impedance at the counter electrode/electrolyte interface (Z_{ce}) and the diffusion and recombination processes occurring at the photoanode (Z_{ph}). These processes are influenced by factors such as the diffusion of triiodide in the electrolyte and the charge transfer resistance associated with electron recombination (Rel).

In particular, Z_{ph} is typically linked with the resistance between electron transport within the photoanode and the charge transfer resistance associated with electron recombination in the electrolyte. By examining these impedance components, researchers can gain insights into the mechanisms governing photoelectron injection and charge recombination dynamics within DSSCs.

The parameters associated with electron transfer in DSSCs were assessed through EIS measurements, and the values obtained for the electrical circuits are listed in Table 2. Figure 6 depicts the experimental Nyquist plots spectrum. In the Nyquist plots (Figure 6), the semicircle near R_{el} represents the Z_{ce} impedance. Both the S:S and S DSSCs exhibit two distinct arcs. Moving from left to right, these arcs correspond to charge transport at the counter electrode/electrolyte interface and the interface between the photoanode-dye and the electrolyte, respectively. However, for the S:S DSSC, only one arc is observed, indicating high impedance at the counter electrode/electrolyte interface. The discrepancy in the arcs positions relative to the origin is attributed to the high electrolyte resistance, likely influenced by solvent properties, the composition of electroactive species, and electrode characteristics.

The equivalent circuit parameters listed in Table 2 reveal that Z_{ph} comprises resistance (R_{ph}) and capacitance (C_p), while Z_{ce} comprises capacitance (C_c) associated with R_{ce}.

Table 2. Equivalent circuit parameters of electronic transport characteristics estimated by EIS for SnO_2-based DSSCs photoanodes.

DSSC	Equivalent Circuit
S:S	$R_{el} = 23.40$ ohm; $R_{ce} = 6.44$ ohm; $R_{ph} = 23.40$ ohm; $C_c = 39.10$ µMho, N = 0.849; $C_p = 1.15$ mMho, N = 0.945
S	$R_{el} = 25.50$ ohm; $R_{ce} = 70.00$ ohm; $R_{ph} = 15.00$ ohm; $C_c = 199.00$ µMho, N = 0.939; $C_p = 30.70$ µMho, N = 0.845
S:C	$R_{el} = 23.40$ ohm; $R_{ce} = 6.44$ ohm; $R_{ph} = 23.40$ ohm; $C_c = 39.10$ µMho, N = 0.849; $C_p = 1.15$ mMho, N = 0.945
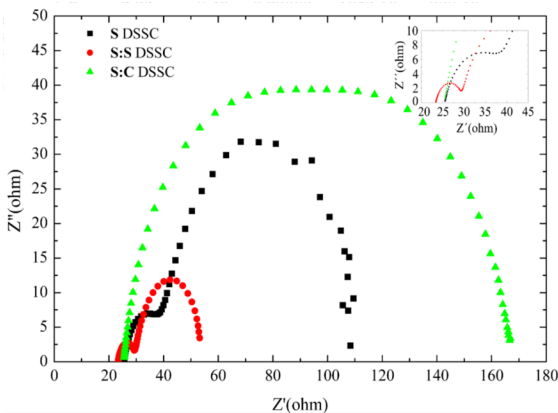
Figure 6. Nyquist graph of the DSSCs: S, S:S and S:C.

The variation in series resistance (R_{el}) is influenced by the electrical contacts of each photovoltaic device.

The charge transport resistance (R_{sh}) increases while R_{ce} decreases, resulting in an increase in electron density in the conduction band of the photoanode and a reduction in inter-resistance. As shown in Table 2, the calculated EIS parameters indicate that the S:S DSSC exhibits low R_{el} and R_{ce} values compared to other cells, contributing to the increased PCE of the S:S DSSC (Table 1). The lower R_{sh} value is reflected in the enhanced PCE of the S:S DSSC.

The equivalent circuit depicted in Table 2 aligns with existing literature on DSSCs, where the values of resistive and capacitive elements are influenced by the type of materials and DSSC configuration. In this study, the R_{ph} value, associated with electron recombination at the photoanode-dye/electrolyte interface, was found to be higher for the S:C DSSC compared to the other cells, resulting in lower efficiency in converting luminous energy to photovoltaic electricity (Table 1).
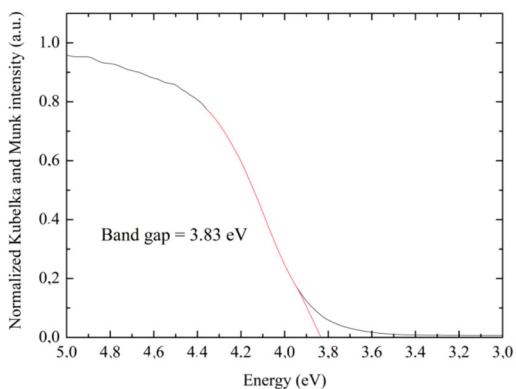
Although the Rph value for the S:S DSSC is higher than that for the S DSSC, this is compensated by the decrease in R_{el} and Z_{ce}. However, this compensation does not occur for the S:C DSSC sample. The dynamics exhibited by the S:S DSSC account for its higher efficiency (PCE = 1.77%) compared to the S and S:C DSSCs. However, the higher value for C_{ph} indicates increased recombination at the photoanode, leading to an increase in Z_{ph}, which in turn reduces cell efficiency.

The lower Jsc value of 2.93 mA.cm^{-2} for the S:C DSSC compared to the S and S:S DSSCs suggests the possibility of increased electron recombination at the SnO_2-CuO grain boundary. Conversely, the higher J_{sc} observed in the S:S DSSC indicates that the high recombination at the interface of the SnO_2 photoanode-dye/electrolyte, integrated into the cell, was counteracted by the increase in open-circuit voltage. This increase provided the necessary energy for photoelectron
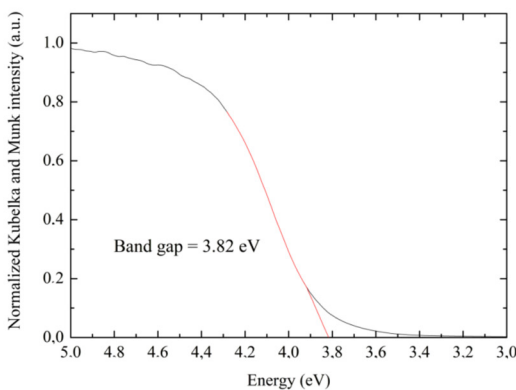
acceleration and reduced electron recombination in the modified SnO_2-SnO_2 grain boundary. Consequently, this led to a decrease in R_{el} and Z_{ce} due to improved ion diffusion in the electrolyte, as shown in Table 2.

The S:S DSSC demonstrates superior efficiency in converting luminous energy into photovoltaic electricity compared to the S, S:B, S:C, and S:NP DSSCs. This is attributed to the favorable electron transport in the conduction band, leading to increased energy conversion efficiency. The presence of numerous oxygen vacancies in the SnO_2 further enhances conductivity in the SnO_2-based photoanodes, resulting in higher J_{sc}. Additionally, the higher R_{ph} value in the S:S DSSC contributes to an increase in V_{oc} compared to the S DSSC. Despite the increase in V_{oc} and R_{ph}, the higher generated photocurrent density offsets these effects in the S:S DSSC.

The photoexcited electrons from the N719 dye molecules are injected into the conduction band of the modified SnO_2 with tin atoms during photoexcitation. These electrons are then transferred to the unmodified SnO_2. This process leads to an excess of electrons in the modified SnO_2 with tin atoms and a downward shift towards the conduction band edge in the grain boundary. As a result, photoexcited electron charge separation is enhanced, leading to improvements in photocurrent and voltage.

The DSSC utilizing the S:S photoanode demonstrates an increase in PCE compared to the S photoanode. To further understand these two photoanodes, Raman spectroscopy and the Kubelka-Munk method were employed. Figure 7 illustrates the Kubelka-Munk plots of the S and S:S photoanodes, derived from diffuse reflectance spectroscopy. The estimated band gap values are 3.83 eV for the S photoanode and 3.82 eV for the S:S photoanode. These values closely align with those reported by Souza and colleagues for pure SnO_2 photoanodes treated at 450°C[38].

The results indicate that it is not feasible to directly correlate the band gap of the S and S:S photoanodes with the tin oxide phases[39,40].

4. Conclusion

The comparison of efficiencies among the DSSCs manufactured in this study highlights the superior performance of the DSSC utilizing a modified SnO_2 photoanode, achieved through the addition of tin salt and subsequent heat treatment at 450°C for 30 minutes. This modification facilitates enhanced charge separation, leading to elevated values of both open circuit voltage (V_{oc}) and short circuit current density (J_{sc}), thereby improving the overall efficiency of the DSSC.

Moving forward, potential future research could involve further characterization of the SnO_2 photoanodes by varying the amount of tin salt and subsequent heat treatment to investigate their effects on the properties and performance of DSSCs. This could provide deeper insights into the optimal conditions for enhancing the efficiency of DSSCs and advancing their potential for practical applications in renewable energy technologies.

5. Acknowledgments

Figure 7. Kubelka and Munk plots: (a) S photoanode and (b) S:S photoanode.

6. References

1. O'Regan B, Grätzel M. A low-cost, high-efficiency solar cell basead on dye-sensitized colloidal TiO_2 films. Nature. 1991;353(6346):737-9.

2. Bandara J, Divarathne CM, Nanayakkara SD. Fabrication of n-p junction electrodes made of n-type SnO_2 and p-type NiO for control of charge recombination in dye sensitized solar cells. Sol Energy Mater Sol Cells. 2004;81(4):429-37.

3. Amalka Perera KAT, Gaveshana Anuradha S, Asoka Kumara GR, Lal Paranawitharana M, Gamini Rajapakse RM, Bandara HMN. The interconnected $CaCO_3$ coated SnO_2 nanocrystalline dye-sensitized solar cell with superior performance. Electrochim Acta. 2011;56(11):4135-8.

4. Chen Z, Tian Y, Li S, Zheng H, Zhang W. Electrodeposition of arborous structure nanocrystalline SnO_2 and application in flexible dye-sensitized solar cells. J Alloys Compd. 2012;515:57-62.

5. Kabre J, LeSuer RJ. Modeling diffusion of tin into the mesoporous titanium dioxide layer of a dye-sensitized solar cell photoanode. J Phys Chem C. 2012;116(34):18327-33.

6. Gong J, Liang J, Sumathy K. Review on dye-sensitized solar cells (DSSCs): fundamental concepts and novel materials. Renew Sustain Energy Rev. 2012;16(8):5848-60.

7. Nagata M, Baldwin E, Kim S, Taya M. Design of dye-sensitized solar cells integrated in composite panel subjected to bending. J Compos Mater. 2012;47(1):27-32.

8. Arai T, Kondo S, Nakano S, Kuramoto T. Performance improvement of a tin(II) dioxide-modified electrode for the dye-sensitized solar cell by the addition of zinc(II) oxide and niobium(V) oxide. Inorg Chim Acta. 2013;395:19-23.

9. Chen L, Li X, Wang Y, Gao C, Zhang H, Zhao B, et al. Low-temperature synthesis of tin dioxide hollow nanospheres and their potential applications in dye-sensitized solar cells and photoelectrochemical type self-powered ultraviolet photodetectors. J Power Sources. 2014;272:886-94.

10. Lim J, Kim HA, Kim BH, Han CH, Jun Y. Reversely fabricated dye-sensitized solar cells. RSC Adv. 2014;4(1):243-7.

11. Dadkhah M, Salavati-Niasari M. Controlled synthesis of tin dioxide nanostructures via two simplemethods and the influence on dye sensitized solar cell. Electrochim Acta. 2014;129:62-8.

12. Shaikh SF, Mane RS, Joo OS. Spraying distance and titanium chloride surface treatment effects on DSSC performance of electrosprayed SnO_2 photoanodes. RSC Adv. 2014;4(68):35919-27.

13. Wang H, Wang B, Yu J, Hu Y, Xia C, Zhang J, et al. Significant enhancement of power conversion efficiency for dye sensitized solar cell using 1D/3D network nanostructures as photoanodes. Sci Rep. 2015;5(9305):1-9.

14. Wali Q, Fakharuddin A, Jose R. Tin oxide as a photoanode for dye-sensitised solar cells: current progress and future challenges. J Power Sources. 2015;293:1039-52.

15. Arote S, Prasad MBR, Tabhane V, Pathan H. Influence of geometrical thickness of SnO_2 based photoanode on the performance of Eosin-Y dye sensitized solar cell. Opt Mater. 2015;49:213-7.

16. Hung IM, Bhattacharjee R. Effect of photoanode design on the photoelectrochemical performance of dye-sensitized solar cells based on SnO_2 nanocomposite. Energies. 2016;9(641):1-11.

17. Chua L, Qin Z, Liu W, Ma X. Inhibition of charge recombination for enhanced dye-sensitized solarcells and self-powered UV sensors by surface modification. Appl Surf Sci. 2016;389:802-9.

18. Batmunkh M, Dadkhah M, Shearer CJ, Biggs MJ, Shapter JG. Incorporation of graphene into SnO_2 photoanodes for dye-sensitized solar cells. Appl Surf Sci. 2016;387:690-7.

19. Arunachalam A, Dhanapandian S, Manoharan C, Bououdina M, Ramalingam G, Rajasekaran M, et al. Influence of sprayed nanocrystalline Zn-doped TiO_2 photoelectrode with the dye extracted from Hibiscus Surattensis as sensitizer in dye- sensitized solar cell. Ceram Int. 2016;42(9):11136-49.

20. Sagaidak I, Huertas G, Nhien ANV, Sauvage F. Towards renewable iodide sources for electrolytes in dye-sensitized solar cells. Energies. 2016;9(241):2-16.

21. Gong J, Sumathy K, Zhou Z, Qiao Q. Modeling of interfacial and bulk charge transfer in dye-sensitized solar cells. Cogent Eng. 2017;4(1287231):1-19.

22. Asemi M, Ghanaatshoar M. Hydrothermal growth of one-dimensional Ce-doped TiO_2 nanostructures for solid-state DSSCs comprising Mg-doped $CuCrO_2$. J Mater Sci. 2017;52(1):489-503.

23. Ozturk T, Gulveren B, Gulen M, Akman E, Sonmezoglu S. An insight into titania nanopowders modifying with manganese ions: a promising route for highly efficient and stable photoelectrochemical solar cells. Sol Energy. 2017;157:47-57.

24. Pereira MS, Lima FAS, Silva CB, Freire PTC, Vasconcelos IF. Structural, morphological and optical properties of SnO_2 nanoparticles obtained by a proteic sol-gel method and their

25. Bu IYY. Novel ZnO decorated SnO_2 nanosheet for dye sensitized solar cell applications. Optik. 2018;157:406-9.

26. Arote SA, Tabhane VA, Pathan HM. Enhanced photovoltaic performance of dye sensitized solar cell using SnO_2 nanoflowers. Opt Mater. 2018;75:601-6.

27. Iqbal MZ, Khan S. Progress in the performance of dye sensitized solar cells by incorporating cost effective counter electrodes. Sol Energy. 2018;160:130-52.

28. Nien YH, Chen HH, Hsu HH, Kuo PY, Chou JC, Hu GM, et al. Enhanced photovoltaic conversion efficiency in dye-sensitized solar cells based on photoanode consisting of TiO_2/GO/Ag nanofibers. Vacuum. 2019;167:47-53.

29. Teixeira ES, Cavalcanti RC, Nunes VF, Maia PHF Jr, Lima FM, Pinho DC, et al. Building and testing a spin coater for the deposition of thin films on DSSCs. Mater Res. 2020;23(6):e20200214.

30. Datta S, Dey A, Singha NR, Roy S. Enhanced performance of dye-sensitized solar cell with thermally stable natural dye-assisted TiO_2/MnO_2 bilayer-assembled photoanode. Mater Renew Sustain Energy. 2020;9(4):1-11.

31. Fegade U, Lin YC, Lin CC, Inamuddin, Wu R-J, Alshahrani B, et al. Spinel oxide incorporated photoanode for better power conversion efficiency in dye-sensitized solar cells. Optik. 2021;247:167976.

32. Cho EJ, Cha JK, Fu G, Cho HS, Lee HW, Kim SH. Selective sensitization strategy for high-performance panchromatic dye-sensitized solar cells incorporated with ruthenium-based double dyes. J Ind Eng Chem. 2022;115:272-8.

33. Alshahrie A, Alghamdi AA, Hasan PMZ, Ahmed F, Albalawi HME, Umar A, et al. Enhancement in the performance of Dye Sensitized Solar Cells (DSSCs) by incorporation of Reduced Graphene Oxide (RGO) and Carbon Nanotubes (CNTs) in ZnO nanostructures. Inorganics. 2022;10(11):204.

34. Swami SK, Kumar N, Radu DR, Cho SW, Lee J. Lithium incorporation into TiO_2 photoanode for performance enhancement of dye-sensitized solar cells. ACS Appl Energy Mater. 2023;6(16):8599-606.

35. Celline AC, Ramadhanti D, Subagja AY, Aprilia A, Safriani L. Improving performance of dye sensitized solar cell (DSSC) by incorporating rGO to TiO_2 based photoanode. AIP Conf Proc. 2023;2604:070006.

36. Ashok A, Beula RJ, Magesh R, Unnikrishnan G, Paul PM, Bennett HC, et al. Bandgap engineering of CuO/TiO_2 nanocomposites and their synergistic effect on the performance of dye-sensitized solar cells. Opt Mater. 2024;148:114896.

37. Ren Y, Zhang D, Suo J, Cao Y, Eickemeyer FT, Vlachopoulos N, et al. Hydroxamic acid pre-adsorption raises the efficiency of cosensitized solar cells. Nature. 2023;613(7942):60-5.

38. Souza APS, Oliveira FGS, Nunes VF, Lima FM, Almeida AFL, Carvalho IMM, et al. High performance SnO_2 pure photoelectrode in dye-sensitized solar cells achieved via electrophoretic technique. Sol Energy. 2020;211:312-23.

39. Eifert B, Becker M, Reindl CT, Giar M, Zheng L, Polity A, et al. Raman studies of the intermediate tin-oxide phase. Phys Rev Mater. 2017;1(1):014602.

40. Alghamdi H, Farinre OZ, Kelley ML, Biacchi AJ, Saha D, Adel T, et al. Experimental spectroscopic data of SnO_2 films and powder. Data. 2023;8(2):37.

41. Nikiforov A, Timofeev V, Mashanov V, Azarov I, Loshkarev I, Volodin V, et al. Formation of SnO and SnO_2 phases during the annealing of SnO (x) films obtained by molecular beam epitaxy. Appl Surf Sci. 2020;512:145735.

42. Mahmood H, Khan MA, Mohuddin B, Iqbal T. Solution-phase growth of tin oxide (SnO_2) nanostructures: structural, optical and photocatalytic properties. Mater Sci Eng B. 2020;258:114568.

43. Habte AG, Hone FG, Dejene FB. Effect of solution pH on structural, optical and morphological properties of SnO_2 nanoparticles. Physica B. 2020;580:411832.

44. Gatea HA. Impact of sintering temperature on crystallite size and optical properties of SnO_2 nanoparticles. J Phys Conf Ser. 2021;1829(1):1.

45. Kajal R, Kataria BR, Asokan K, Mohan D. Effects of gamma radiation on structural, optical, and electrical properties of SnO_2 thin films. Applied Surf Sci Adv. 2023;15:100406.

46. Sambasivam S, Obaidat IM. Effect of iron doping on ESR and Raman spectra of SnO_2 nanomaterials. Mater Today Proc. 2020;28:587-90.

47. Alghamdi H, Farinre OZ, Kelley ML, Biacchi AJ, Saha D, Adel T, et al. Experimental spectroscopic data of SnO_2 films and powder. Data. 2023;8(2):37.

48. Singha KK, Singh PP, Narzary R, Mondal A, Gupta M, Sathe VG, et al. Crystal structure, Raman spectroscopy and optical property study of Mg-Doped SnO_2 compounds for optoelectronic devices. Crystals. 2023;13(6):932.

49. Singha KK, Mondal A, Gupta M, Sathe VG, Kumar D, Srivastava SK. Investigations of structural, optical and transport property of Sb-doped SnO_2 compounds for optoelectronics application. Optik. 2023;288:171210.

50. Aimukhanov AK, Seisembekova TE, Zeinidenov AK, Kambar DS. The impact of SnO_2 photoelectrode's thickness on photovoltaic properties of the solar cell FTO: SnO_2: PTB7-TH: ITIC/Mo/Ag. Bull Karaganda Univ Phys Ser. 2022;106(2):86-91.